

# Ubiquity of Exciton Localization in Cryogenic Carbon Nanotubes

Matthias S. Hofmann,<sup>†</sup> Jonathan Noé,<sup>†</sup> Alexander Kneer,<sup>†</sup> Jared J. Crochet,<sup>‡</sup> and Alexander Högele<sup>\*,†</sup>

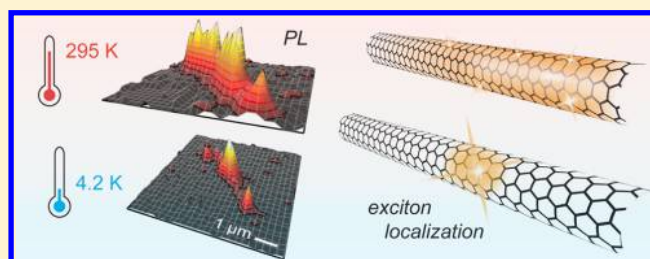
<sup>†</sup>Fakultät für Physik, Munich Quantum Center, and Center for NanoScience (CeNS), Ludwig-Maximilians-Universität München, Geschwister-Scholl-Platz 1, D-80539 München, Germany

<sup>‡</sup>Physical Chemistry and Applied Spectroscopy Division, Los Alamos National Laboratory, Los Alamos, New Mexico 87545, United States

**S** Supporting Information

**ABSTRACT:** We present photoluminescence studies of individual semiconducting single-wall carbon nanotubes at room and cryogenic temperatures. From the analysis of spatial and spectral features of nanotube photoluminescence, we identify characteristic signatures of unintentional exciton localization. Moreover, we quantify the energy scale of exciton localization potentials as ranging from a few to a few tens of millielectronvolts and stemming from both environmental disorder and shallow covalent side-wall defects. Our results establish disorder-induced crossover from the diffusive to the localized regime of nanotube excitons at cryogenic temperatures as a ubiquitous phenomenon in micelle-encapsulated and as-grown carbon nanotubes.

**KEYWORDS:** Carbon nanotube, photoluminescence spectroscopy, exciton localization



Semiconducting single-wall carbon nanotubes (CNTs) exhibit chirality-specific absorption in the visible<sup>1</sup> and emission in the near-infrared<sup>2</sup> as premises to a wide range of optoelectronic applications.<sup>3</sup> By virtue of strong Coulomb interactions, the motion of the photogenerated electrons and holes along the nanotube axis is correlated and gives rise to exciton<sup>4,5</sup> diffusion dynamics at room temperature.<sup>6–17</sup> At cryogenic temperatures, however, individual CNTs exhibit single-photon emission statistics<sup>18</sup> as a hallmark of exciton localization.<sup>18–25</sup> This quasi zero-dimensional regime of CNTs is of both fundamental and practical interest, as it provides improved coherence<sup>23,24</sup> and higher quantum yield<sup>25,26,27</sup> of localized excitons for novel applications in quantum cryptography<sup>18,22–24,28</sup> or spin-based quantum information processing.<sup>29</sup>

Exciton localization can arise accidentally in various CNT materials,<sup>18–20,22–25</sup> or it can be promoted by means of covalent side-wall functionalization with oxygen<sup>26,28,30,31</sup> or diazonium<sup>27</sup> chemistry. While chemical doping yields defect-specific exciton localization traps as deep as 100–300 meV,<sup>26–28,30,31</sup> the order of magnitude of unintentional localization potentials stemming from structural or environmental disorder along the CNT axis remained elusive. In the following, we present the results of photoluminescence (PL) spectroscopy experiments on single CNTs identifying the localization energy scale and the related spectral signatures of disorder-induced exciton traps. Our comprehensive studies are based on monitoring the PL of individual micelle-encapsulated HiPco and CoMoCAT nanotubes, as well as CNTs obtained with in-house chemical vapor deposition (CVD) on silica substrates (see *Methods*) at room temperature (295 K) and the

temperatures of liquid nitrogen (77 K) and liquid helium (4.2 K).

## RESULTS AND DISCUSSION

First we establish the characteristic spectral signatures of unintentional exciton localization using a representative CNT of several microns in length. The atomic force micrograph in *Figure 1a* shows the respective HiPco CNT with a length of  $\sim 10 \mu\text{m}$  and a diameter of  $\sim 0.8 \text{ nm}$  determined from the height profile in *Figure 1b*. For the same nanotube we recorded hyperspectral maps at three fixed temperatures by raster-scanning the sample with respect to the focal spot of an apochromatic low-temperature micro-objective and recording the PL spectrum within the interval of 1.20–1.30 eV at each pixel. The corresponding raster-scan PL intensity images shown in *Figure 1c–e* were obtained by integrating the spectra within limited exciton-specific bands at each pixel. The profiles of the PL intensity (*Figure 1f–h*) and the spectral PL characteristics (*Figure 1i–k*) were obtained from respective hyperspectral image analysis along the nanotube axis.

At room temperature, the (7,5) nanotube of *Figure 1a* exhibited a PL resonance consistently centered at 1.207 eV<sup>2,32</sup> with  $\sim 30 \text{ meV}$  full-width at half-maximum (FWHM) line width and without significant spectral variations along the nanotube axis (*Figure 1i*). The respective axial PL intensity profile was extended over several microns (*Figure 1f*) with characteristic

**Received:** December 1, 2015

**Revised:** March 29, 2016

**Published:** April 22, 2016

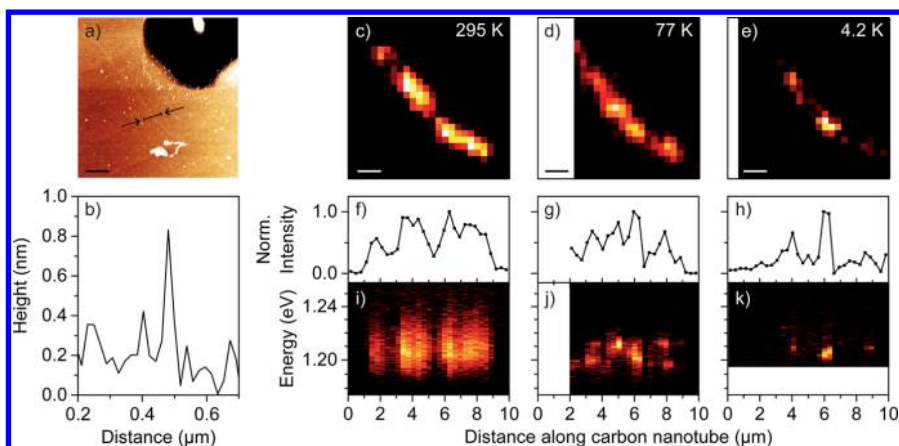


**Figure 1.** (a) Atomic force micrograph of a single HiPco carbon nanotube with a length of  $\sim 10 \mu\text{m}$ . The black area in the upper right corner is an etched marker structure. (b) The height profile along the line in the topography image in (a) is consistent with the diameter of an individual (7,5) nanotube. (c,d,e) Local photoluminescence maps of the same sample area as in (a). (f,g,h) Intensity profiles along the nanotube axis at temperatures of 295, 77, and 4.2 K. The nanotube exhibits extended room-temperature emission that fractionalizes progressively into emission hot-spots at cryogenic temperatures. (i,j,k) The spectral dispersion of the photoluminescence energy along the carbon nanotube axis at three fixed temperatures of the experiment reveals the emergence of multipeak emission upon cool-down. The scale bars are  $1 \mu\text{m}$ .

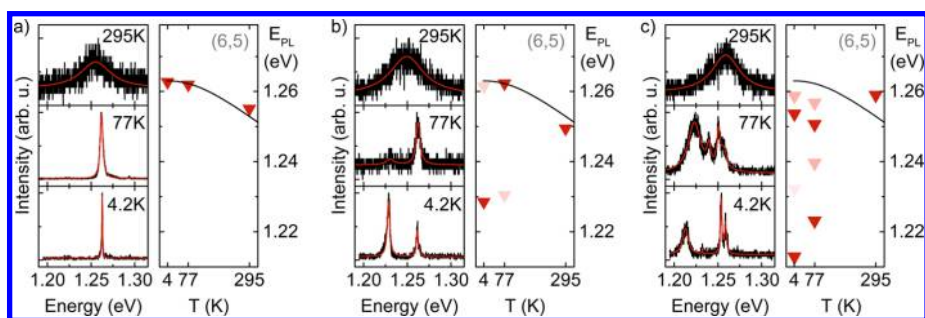


**Figure 2.** (a) Photoluminescence spectra of an individual (6,5) HiPco carbon nanotube at 295, 77, and 4.2 K (left panel) and peak emission energies  $E_{\text{PL}}$  (right panel) extracted from Lorentzian fits (red solid lines). The energy dispersion with temperature (black solid line) shows the theoretical dependence of the band gap according to Capaz et al.<sup>36</sup> (b,c) Same data for two other (6,5) HiPco carbon nanotubes of the sample that deviate from the ideal picture by developing red-shifted satellites of multipeak spectra. Data points with different shades of red indicate relative intensities of the emission peaks.

quenching regions at the nanotube ends and at the sites of disorder sampled by diffusive excitons.<sup>6–17</sup> The fragmented axial PL profile at ambient conditions fractionalized progressively with reduced temperatures. The raster-scan images in Figure 1d,e, as well as the axial PL profiles in Figure 1g,h, demonstrate how the extended nanotube PL evolved into singular hot-spots at 77 and 4.2 K, respectively. This hot-spot axial PL fragmentation, observed with confocal microscopy for cryogenic nanotubes, is one main signature of exciton localization at the sites of disorder that resembles previous observations at room temperature and sub-100 nm length scales with near-field microscopy.<sup>8,33</sup> The second main signature is evidenced by the spectral axial PL profiles of Figure 1j,k: the spectral variations of 10–15 meV along the CNT axis<sup>33</sup> become more and more pronounced on the scale of the spectral line width of  $\sim 3$  meV and  $\sim 1$  meV at the temperatures of liquid nitrogen and liquid helium, respectively. Finally, we identify the emergence of multiple emission resonances (as in Figure 1j at the axial position of  $8 \mu\text{m}$ ) as the third main characteristic of exciton localization in accord with previous studies.<sup>34,35</sup>

In the second step of our analysis, we use the multipeak PL structure of individual nanotubes to quantify the energy scale associated with unintentional exciton trap potentials. To this

end we confront our experimental observations at three fixed points of temperature with theoretical expectations. The data in Figure 2a exemplifies our approach. The spectra of a single (6,5) HiPco nanotube at 295, 77, and 4.2 K were used to extract the PL peak positions from Lorentzian fits (red lines in the left panel of Figure 2a) as a function of temperature, and to compare these values for the emission energies (triangles in the right panel of Figure 2a) with the theoretical prediction for the thermal band gap renormalization<sup>36</sup> (black solid lines in the right panel of Figure 2a). As for the nanotube in Figure 2a, we assigned the chirality to individual CNTs of our experiments using their room temperature PL emission energy<sup>2,32</sup> and allowing energy offsets of the order of 10–20 meV to account for the tube-to-tube variations in the effective dielectric environment<sup>37–39</sup> which may stem from an inhomogeneous tube coverage by surfactant,<sup>15</sup> water-filling of CNTs dispersed from aqueous suspensions,<sup>40</sup> or local charges in the nearby substrate.<sup>35,41,42</sup>

Figure 2b,c shows data of two other (6,5) HiPco nanotubes of the same sample. Both tubes clearly contrast the nearly ideal picture of the CNT in Figure 2a: instead of the expected line narrowing and blue-shift upon cool-down, they develop multipeak PL resonances (two and four peaks in the spectra of Figure 2b,c, respectively) of variable line widths (note the

broad red-most peak in Figure 2c) and spectral red-shifts of the order of a few tens of millielectronvolts. In the case of the two-peak emission, the fundamental PL peak follows the theoretically expected energy dispersion but loses its intensity at the expense of the red-shifted satellite that emerges as a weak signature at 77 K and dominates at 4.2 K (Figure 2b). This observation is consistent with thermal localization of excitons in the lowest-lying state, which appears 33 meV below the fundamental exciton emission  $E_{11}$  for the CNT of Figure 2b. The example of a CNT with a four-peak emission as in Figure 2c is also instructive. The energy splittings between the satellites and the main  $E_{11}$  peak, that roughly follows the theoretical thermal shift, were estimated as 5, 26, and 46 meV from Lorentzian fits to the spectra at 4.2 K in Figure 2c. This energy scale is in remarkable agreement with the low-temperature characteristics of shallow oxygen side-wall defects in ether-I configuration.<sup>31</sup> Although the agreement could be accidental and deeper-lying localization states established in previous spectroscopy of oxygen-doped CNTs<sup>26,28,30,31</sup> were not observed in our experiments due to the limited spectral detection window, it is plausible to include the class of covalent side-wall defects as a likely source of unintentional exciton localization. The fact that none of the CNTs on our samples have experienced a deliberate chemical treatment prior to spectroscopic studies, yet in most cases exhibited multiplex spectra, indicates that the notion of one-dimensional diffusive excitons in cryogenic CNTs is of only limited validity.

In order to establish the generality of this finding, we analyzed individual CNTs with single-peak spectra at room temperature and multiplex spectra at cryogenic conditions. The procedure described above allows us to quantify the exciton localization energy scale for CNTs of different chiralities obtained with different synthesis methods. Figure 3a–d shows the histograms of PL peak energies for HiPco tubes of (6,5) and (8,3) chirality, CoMoCAT (6,5) and as-grown (9,1) CNTs, respectively. We emphasize that only the fraction of

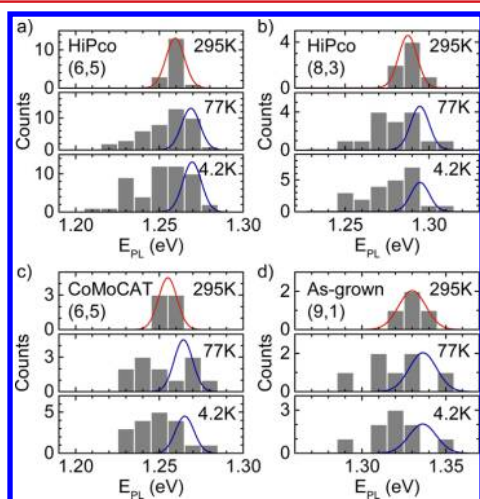


**Figure 3.** Photoluminescence energy histograms of (a) HiPco (6,5), (b) HiPco (8,3), (c) CoMoCAT (6,5) and (d) as-grown (9,1) carbon nanotubes at 295, 77, and 4.2 K. The Gaussian distributions of the single-peak emission at 295 K with  $\sim 10$ – $20$  meV full-widths at half-maxima (red solid lines) were used to calculate theoretically expected cryogenic distributions (blue solid lines) by taking into account the thermal band gap renormalization after Capaz et al.<sup>36</sup> Both the broadening and the asymmetry of the experimental distributions at cryogenic temperatures stem from exciton localization.

CNTs with a single PL peak at room temperature was selected for statistical analysis. The increase in occurrences at cryogenic temperatures is a direct consequence of multiplex emission profiles attributed to incidental localization. For each chirality and CNT synthesis method, we fitted the ensemble distribution of the PL energies at 295 K with a Gaussian function (shown as red solid lines in Figure 3) centered at the corresponding room-temperature energy of the chirality-specific  $E_{11}$  with a FWHM of 13 meV for the HiPco tubes and the (6,5) CoMoCAT tubes, and 19 meV for the as-grown (9,1) CNTs. Same FWHMs of micelle-encapsulated HiPco and CoMoCAT CNTs reflect similar average dielectric environments of nanotubes on samples prepared out of aqueous suspensions, while as-grown CNTs without surfactant are likely to experience higher spectral fluctuations and thus ensemble broadening due to their proximity to charge traps in  $\text{SiO}_2$ . In the low-temperature PL histograms of Figure 3 the Gaussian ensemble distributions (blue solid lines) were blue-shifted according to the theoretical temperature dependence of the band gap.<sup>36</sup>

The asymmetric cryogenic ensemble distributions of Figure 3 underpin the picture of lower-lying exciton trap states, discussed above at the level of individual nanotubes. Furthermore, they provide evidence for unintentional exciton localization as a universal feature of CNT materials: for micelle-encapsulated HiPco and CoMoCAT CNTs as well as for surfactant-free as-grown nanotubes, we observed a redistribution of the PL emission from the fundamental  $E_{11}$  transition at room temperature to lower-lying localized exciton states at cryogenic temperatures. The higher energy tail of the Gaussian ensemble distribution at 295 K is depleted upon cool-down, while the occurrence of the PL emission peaks at the lower energy side increases—a signature of exciton localization by environmental disorder with trap potentials as deep as 50–60 meV (lowest-energy states of (6,5) HiPco tubes at 4.2 K in Figure 3a).

To shed light on the nature of the environmental disorder caused by adsorbates on the nanotube surface we present in Figure 4 a set of data for a single as-grown (9,1) CNT recorded over several cooling cycles. All PL measurements were carried out on the same CNT in the inert atmosphere of a helium gas at 20 mbar. However, the sample had been exposed to ambient conditions for several days before the second cooling cycle, as indicated in the illustration of the measurement procedure shown in Figure 4a. After a measurement point at 77 K, the CNT was sampled twice from 295 to 4.2 K with a measurement point at 77 K in between, and the maxima of the PL emission energy were determined at each fixed temperature point (colored data points in Figure 4b). The first red-shift of 2 meV in the PL energy from 77 to 295 K is consistent with the thermal band gap renormalization of 6 meV expected for a (9,1) CNT.<sup>36</sup> Instead of blue-shifting back upon temperature reversal, however, the CNT PL developed a red-shift of 24 meV indicated by the first arrow in Figure 4b. We interpret this red-shift as arising from a modified dielectric environment of the CNT due to adsorbates,<sup>39,43–46</sup> most likely oxygen or nitrogen, that have contaminated the nanotube surface during its exposure to ambient conditions.

A further cool-down step from 77 to 4.2 K in the inert helium atmosphere added an additional red-shift of 9 meV (second arrow in Figure 4b) instead of the theoretically expected value of 0.3 meV. It is plausible that additional adsorption of oxygen or nitrogen, both present in their gaseous phase at 77 K and 20 mbar as a remanent contamination of the

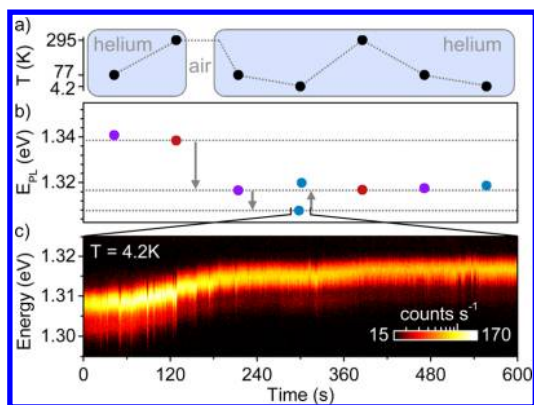


**Figure 4.** (a) Measurement procedure: the emission of a single as-grown nanotube in an inert helium atmosphere was sampled at three fixed temperature points (the measurement progress was from left to right). After the first measurement point at 295 K, the sample was exposed to air under ambient conditions. (b) Corresponding peak photoluminescence energy  $E_{PL}$  determined at each point of fixed temperatures (red, purple, and blue circles represent data points at 295, 77, and 4.2 K, respectively). (c) False-color representation of the photoluminescence evolution at 4.2 K over 10 min. The emission energy exhibited a blue-shift of  $\sim 10$  meV during the course of the measurement. The laser power density was  $17 \text{ kW/cm}^2$  at 807 nm wavelength.

helium atmosphere, was responsible for this second red-shift. This scenario is supported by the observation of a laser-induced desorption process (third arrow in Figure 4b), which we monitored in situ with cryogenic PL spectroscopy. Figure 4c shows a sequence of 10 min as a part of this process: the temporal evolution of the nanotube PL showed a blue-shift of the emission energy by 12 meV due to desorption<sup>43</sup> induced by local laser heating. Within the initial  $\sim 5$  min of laser excitation with a power density of  $17 \text{ kW/cm}^2$  at 807 nm wavelength, the PL energy leveled-off at 1.32 eV after overcompensating for the red-shift caused previously by molecule adsorption at cryogenic conditions. Successive heating and cooling cycles showed thermally induced PL blue- and red-shifts within the range of a few millielectronvolts (last four data points in Figure 4b) in accord with theoretical expectations. The observation of the PL energy shifts of the order of a few tens of millielectronvolts caused by adsorption and desorption processes on the very same CNT highlight the role that environmental disorder can play in exciton localization: an inhomogeneous coverage of the CNT surface by adsorbates would result in local exciton traps with potentials comparable to those of shallow covalent sidewall defects.

In summary, our results establish exciton localization as a general feature of micelle-encapsulated and as-grown CNTs at low temperatures and can be generalized to other low-dimensional semiconductors with large surface-to-volume ratios, including the emergent class of transition metal dichalcogenides. The analysis of spectral signatures, both at the level of individual nanotubes and CNT ensembles in different materials, highlights the roles of crystalline and environmental disorder for cryogenic exciton localization. Our findings not only emphasize the sensitivity of the CNT excitons to their immediate surrounding, they also indicate the potential for spectral fine-tuning of the CNT emission into resonance with fiber-based optical microcavities<sup>47,48</sup> for the realization of efficient single-photon cryptography devices in the telecom transmission window.

## METHODS

**Sample Preparation.** Si/SiO<sub>2</sub> substrates were used to support HiPco and CoMoCAT CNTs wrapped in deoxycholate and sodium cholate, respectively. Prior to the dispersion of HiPco and CoMoCAT CNTs out of aqueous suspensions the substrates were patterned with markers for lateral orientation on the sample by direct optical imaging or by monitoring the intensity of the silicon Raman band at  $521 \text{ cm}^{-1}$ . The markers were fabricated by optical lithography and successive reactive ion etching or metal deposition. Surfactant-wrapped HiPco and CoMoCAT CNTs were spin-coated on the substrates to yield densities of less than one nanotube per  $\mu\text{m}^2$ . For samples with as-grown CNTs, we used commercial TEM grids consisting of a silicon nitride membrane with a perforated coordinate system. A 100 nm thick SiO<sub>2</sub>-layer was deposited on the TEM grids by plasma-enhanced chemical vapor deposition prior to the synthesis of CNTs.

**Chemical Vapor Deposition of CNTs.** As-grown CNTs were synthesized in a home-built chemical vapor deposition furnace. A bimetallic iron–ruthenium catalyst was drop-casted from a suspension onto TEM grids coated with SiO<sub>2</sub>. Successively, the samples were placed in the CVD furnace and heated to  $850 \text{ }^\circ\text{C}$  in an argon/hydrogen-flow. The gas flow was successively switched to methane and hydrogen for 10 min for CNT synthesis. The samples were cooled to  $\leq 300 \text{ }^\circ\text{C}$  under argon/hydrogen flow before unloading.

**Photoluminescence Microscopy and Spectroscopy.** Photoluminescence experiments were performed in a home-built cryogenic confocal microscope. The samples were mounted on piezo-stepping and -scanning units (*attocube systems* ANPxyz101 and ANSxy100) for positioning with respect to the confocal excitation and detection spots of a low-temperature apochromatic objective (*attocube systems* LT-APO/NIR/075) with a diffraction limited spot of  $1 \mu\text{m}$ . The microscope unit with the objective and the sample was placed in a dewar with an inert helium atmosphere at a pressure of 20 mbar and was either kept at room temperature or immersed in liquid nitrogen (77 K) or liquid helium (4.2 K) in a bath cryostat. Excitation around 790–850 nm was performed with a wavelength-tunable Ti:sapphire laser system (*Coherent Mira*) in continuous wave mode. The PL was spectrally dispersed by a monochromator (*Princeton Instruments* Acton SP-2558 or –2750) and detected with a nitrogen-cooled silicon CCD (*Princeton Instruments* Spec-10:100BR/LN). Typical integration times were in the range of 1–30 s.

## ASSOCIATED CONTENT

### Supporting Information

The Supporting Information is available free of charge on the ACS Publications website at DOI: [10.1021/acs.nanolett.5b04901](https://doi.org/10.1021/acs.nanolett.5b04901).

Complementary to the data in Figure 2, additional photoluminescence spectra as well as photoluminescence peak positions and their theoretical temperature dependence are presented for individual HiPco, CoMoCAT, and as-grown carbon nanotubes at three fixed points of temperature (295, 77, and 4.2 K). (PDF)

## AUTHOR INFORMATION

### Corresponding Author

\*E-mail: [alexander.hoegele@lmu.de](mailto:alexander.hoegele@lmu.de).

## Notes

The authors declare no competing financial interest.

## ■ ACKNOWLEDGMENTS

We thank P. Altpeter and R. Rath for assistance in the clean room. The preparation of HiPco nanotube samples was performed in part at the Center for Integrated Nanotechnologies, Los Alamos National Laboratory. This research was funded by the European Research Council under the ERC Grant Agreement no. 336749, and the German Excellence Initiative via the Nanosystems Initiative Munich (NIM). We also acknowledge financial support from the Center for NanoScience (CeNS) and LMUinnovativ.

## ■ REFERENCES

- (1) O'Connell, M. J.; Bachilo, S. M.; Huffman, C. B.; Moore, V. C.; Strano, M. S.; Haroz, E. H.; Rialon, K. L.; Boul, P. J.; Noon, W. H.; Kittrell, C.; Ma, J.; Hauge, R. H.; Weisman, R. B.; Smalley, R. E. *Science* **2002**, *297*, 593–596.
- (2) Bachilo, S. M.; Strano, M. S.; Kittrell, C.; Hauge, R. H.; Smalley, R. E.; Weisman, R. B. *Science* **2002**, *298*, 2361–2366.
- (3) Avouris, P.; Freitag, M.; Perebeinos, V. *Nat. Photonics* **2008**, *2*, 341–350.
- (4) Wang, F.; Dukovic, G.; Brus, L. E.; Heinz, T. F. *Science* **2005**, *308*, 838–841.
- (5) Maultzsch, J.; Pomraenke, R.; Reich, S.; Chang, E.; Prezzi, D.; Ruini, A.; Molinari, E.; Strano, M. S.; Thomsen, C.; Lienau, C. *Phys. Rev. B: Condens. Matter Mater. Phys.* **2005**, *72*, 241402.
- (6) Cognet, L.; Tsyboulski, D. A.; Rocha, J.-D. R.; Doyle, C. D.; Tour, J. M.; Weisman, R. B. *Science* **2007**, *316*, 1465–1468.
- (7) Lüer, L.; Hoseinkhani, S.; Polli, D.; Crochet, J.; Hertel, T.; Lanzani, G. *Nat. Phys.* **2009**, *5*, 54–58.
- (8) Georgi, C.; Böhmeler, M.; Qian, H.; Novotny, L.; Hartschuh, A. *Phys. Status Solidi B* **2009**, *246*, 2683–2688.
- (9) Moritsubo, S.; Murai, T.; Shimada, T.; Murakami, Y.; Chiashi, S.; Maruyama, S.; Kato, Y. K. *Phys. Rev. Lett.* **2010**, *104*, 247402.
- (10) Yoshikawa, K.; Matsuda, K.; Kanemitsu, Y. *J. Phys. Chem. C* **2010**, *114*, 4353–4356.
- (11) Hertel, T.; Himmelein, S.; Ackermann, T.; Stich, D.; Crochet, J. *ACS Nano* **2010**, *4*, 7161–7168.
- (12) Harrah, D. M.; Swan, A. K. *ACS Nano* **2011**, *5*, 647–655.
- (13) Xie, J.; Inaba, T.; Sugiyama, R.; Homma, Y. *Phys. Rev. B: Condens. Matter Mater. Phys.* **2012**, *85*, 085434.
- (14) Siitonen, A. J.; Bachilo, S. M.; Tsyboulski, D. A.; Weisman, R. B. *Nano Lett.* **2012**, *12*, 33–38.
- (15) Crochet, J. J.; Duque, J. G.; Werner, J. H.; Lounis, B.; Cognet, L.; Doorn, S. K. *Nano Lett.* **2012**, *12*, 5091–5096.
- (16) Oudjedi, L.; Parra-Vasquez, A. N. G.; Godin, A. G.; Cognet, L.; Lounis, B. *J. Phys. Chem. Lett.* **2013**, *4*, 1460–1464.
- (17) Ishii, A.; Yoshida, M.; Kato, Y. K. *Phys. Rev. B: Condens. Matter Mater. Phys.* **2015**, *91*, 125427.
- (18) Högele, A.; Galland, C.; Winger, M.; Imamoğlu, A. *Phys. Rev. Lett.* **2008**, *100*, 217401.
- (19) Htoon, H.; O'Connell, M. J.; Cox, P. J.; Doorn, S. K.; Klimov, V. I. *Phys. Rev. Lett.* **2004**, *93*, 027401.
- (20) Hirori, H.; Matsuda, K.; Miyauchi, Y.; Maruyama, S.; Kanemitsu, Y. *Phys. Rev. Lett.* **2006**, *97*, 257401.
- (21) Galland, C.; Högele, A.; Türeci, H. E.; Imamoğlu, A. *Phys. Rev. Lett.* **2008**, *101*, 067402.
- (22) Walden-Newman, W.; Sarpkaya, I.; Strauf, S. *Nano Lett.* **2012**, *12*, 1934–1941.
- (23) Hofmann, M. S.; Glückert, J. T.; Noé, J.; Bourjau, C.; Dehmel, R.; Högele, A. *Nat. Nanotechnol.* **2013**, *8*, 502–505.
- (24) Sarpkaya, I.; Zhang, Z.; Walden-Newman, W.; Wang, X.; Hone, J.; Wong, C. W.; Strauf, S. *Nat. Commun.* **2013**, *4*, 2152.
- (25) Violla, F.; Chassagneux, Y.; Ferreira, R.; Roquelet, C.; Diederichs, C.; Cassabois, G.; Roussignol, P.; Lauret, J. S.; Voisin, C. *Phys. Rev. Lett.* **2014**, *113*, 057402.
- (26) Miyauchi, Y.; Iwamura, M.; Mouri, S.; Kawazoe, T.; Ohtsu, M.; Matsuda, K. *Nat. Photonics* **2013**, *7*, 715–719.
- (27) Piao, Y.; Meany, B.; Powell, L. R.; Valley, N.; Kwon, H.; Schatz, G. C.; Wang, Y. *Nat. Chem.* **2013**, *5*, 840–845.
- (28) Ma, X.; Hartmann, N. F.; Baldwin, J. K. S.; Doorn, S. K.; Htoon, H. *Nat. Nanotechnol.* **2015**, *10*, 671–675.
- (29) Galland, C.; Imamoğlu, A. *Phys. Rev. Lett.* **2008**, *101*, 157404.
- (30) Ghosh, S.; Bachilo, S. M.; Simonette, R. A.; Beckingham, K. M.; Weisman, R. B. *Science* **2010**, *330*, 1656–1659.
- (31) Ma, X.; Adamska, L.; Yamaguchi, H.; Yalcin, S. E.; Tretiak, S.; Doorn, S. K.; Htoon, H. *ACS Nano* **2014**, *8*, 10782–10789.
- (32) Weisman, R. B.; Bachilo, S. M. *Nano Lett.* **2003**, *3*, 1235–1238.
- (33) Georgi, C.; Green, A. A.; Hersam, M. C.; Hartschuh, A. *ACS Nano* **2010**, *4*, 5914–5920.
- (34) Lefebvre, J.; Finnie, P.; Homma, Y. *Phys. Rev. B: Condens. Matter Mater. Phys.* **2004**, *70*, 045419.
- (35) Matsuda, K.; Inoue, T.; Murakami, Y.; Maruyama, S.; Kanemitsu, Y. *Phys. Rev. B: Condens. Matter Mater. Phys.* **2008**, *77*, 193405.
- (36) Capaz, R. B.; Spataru, C. D.; Tangney, P.; Cohen, M. L.; Louie, S. G. *Phys. Rev. Lett.* **2005**, *94*, 036801.
- (37) Lefebvre, J.; Fraser, J.; Homma, Y.; Finnie, P. *Appl. Phys. A: Mater. Sci. Process.* **2004**, *78*, 1107–1110.
- (38) Ohno, Y.; Iwasaki, S.; Murakami, Y.; Kishimoto, S.; Maruyama, S.; Mizutani, T. *Phys. Rev. B: Condens. Matter Mater. Phys.* **2006**, *73*, 235427.
- (39) Miyauchi, Y.; Saito, R.; Sato, K.; Ohno, Y.; Iwasaki, S.; Mizutani, T.; Jiang, J.; Maruyama, S. *Chem. Phys. Lett.* **2007**, *442*, 394–399.
- (40) Cambré, S.; Santos, S. M.; Wenseleers, W.; Nugraha, A. R. T.; Saito, R.; Cognet, L.; Lounis, B. *ACS Nano* **2012**, *6*, 2649–2655.
- (41) Ai, N.; Walden-Newman, W.; Song, Q.; Kalliakos, S.; Strauf, S. *ACS Nano* **2011**, *5*, 2664–2670.
- (42) Ma, X.; Roslyak, O.; Wang, F.; Duque, J. G.; Piryatinski, A.; Doorn, S. K.; Htoon, H. *ACS Nano* **2014**, *8*, 10613–10620.
- (43) Finnie, P.; Homma, Y.; Lefebvre, J. *Phys. Rev. Lett.* **2005**, *94*, 247401.
- (44) Choi, J. H.; Strano, M. S. *Appl. Phys. Lett.* **2007**, *90*, 223114.
- (45) Araujo, P. T.; Jorio, A. *Phys. Status Solidi B* **2008**, *245*, 2201–2204.
- (46) Chiashi, S.; Watanabe, S.; Hanashima, T.; Homma, Y. *Nano Lett.* **2008**, *8*, 3097–3101.
- (47) Jeantet, A.; Chassagneux, Y.; Raynaud, C.; Roussignol, P.; Lauret, J.-S.; Besga, B.; Estève, J.; Reichel, J.; Voisin, C. Widely tunable single-photon source from a carbon nanotube in the Purcell regime. *arXiv* **2015**, arXiv:1508.06297v1.
- (48) Hümmel, T.; Noé, J.; Hofmann, M. S.; Hänsch, T. W.; Högele, A.; Hunger, D. Cavity-enhanced Raman Microscopy of Individual Carbon Nanotubes. *arXiv* **2015**, arXiv:1508.06810v1.